River Flow 2006 – Ferreira, Alves, Leal & Cardoso (eds)
© 2006 Taylor & Francis Group, London, ISBN 0-415-40815-6

Accurate measurements of free-surface in the dam-break problem

Steve Cochard & Christophe Ancey
École Polytechnique Fédérale de Lausanne

ABSTRACT: The dam-break problem (i.e. the sudden release of a given volume of fluid along a slope) has attracted much attention from mechanicians and physicists over the last years. Of particular interest are the free-surface profile and the spreading rate. From the experimental viewpoint, impediments to accurate measurements of the free-surface evolution are many because of the significant variations in its curvature and velocity.

In order to accurately measure the free-surface variations (position, flow depth profile, leading edge, surface velocity) of a high-speed surge, a new imaging system has been developed at EPFL. The imaging system consists of a digital camera coupled with a synchronised micro-mirrors projector. The object surface is imaged into a camera and patterns are projected onto the surface under an angle of incidence that differs from the imaging direction. From the deformed pattern recorded by the camera, phase can be extracted and, by using unwrapping algorithms, height can be computed and the free surface is reconstructed. We measure the free surface of the flow to within 0.1 mm over a surface of $1.8 \times 1.1\ \mathrm{m}^2$.

1 INTRODUCTION

Shallow-water equations have been originally designed by saint venant (1871) to compute flood propagation along rivers. Their use was gradually extended to strongly time-dependent flows such as waves induced by a dam break (Ritter 1892). There is currently a growing number of models based on the shallow-water equations, which are used to describe natural flows such as flash floods (Hogg and Pritchard 2004), floods with sediment transport (Pritchard 2005), snow avalanches (Bartelt et al. 1999), debris flows (Iverson 1997; Huang and Garcìa 1997), lava flows (Griffiths 2000), subaqueous avalanches (Parker et al. 1986), etc. In the derivation of these models, a number of assumptions are used, the most important of which are: the long-wave approximation (no significant curvature of the free surface), hydrostatic pressure, blunt velocity profile, and no change in the bulk composition or rheology. Furthermore, in these models, the bottom shear stress is computed using either *ad hoc* expressions (e.g., Chézy friction) or non-Newtonian constitutive equations, with the difficult question of parameter fitting. Given the number of approximations and assumptions needed for obtaining these models, one can be legitimately be suspicious about their reliability and performance.

Essentially, our idea was to test the shallow-flow equations under extreme conditions in a well controlled environment—the laboratory—, where both the initial and boundary conditions are prescribed. Here, ‘extreme conditions’ mean that we focus our attention on time-dependent flows (surges with a front) mobilizing non-Newtonian fluids, experiencing different stages from release to run-out: acceleration (balance between inertia and pressure gradient), nearly fully developed regime (flow at equilibrium), and deposition (prevalence of dissipation processes). Preliminary experiments are run with viscoplastic materials.

The objective of this paper is to describe the experimental facilities and procedures. Emphasis is given to accurate reconstruction of three-dimensional flow depth profiles. These measurements are particularly difficult to perform, especially when fastness and accuracy are sought. Various techniques have been proposed over the last years (e.g., laser probe, videogrammetry). For our purpose, we have used image-processing techniques based on the projection of patterns (Desmangles 2003). In the following, we will describe the technique adapted to our particular case and provide an example of application.

2 FACILITY AND PROCEDURES

2.1 *Overview*

Figure 1 shows the experimental setup. The typical procedure is the following. A viscoplastic fluid is placed in a reservoir on the top of an inclined plane. The fluid is suddenly released by opening the dam

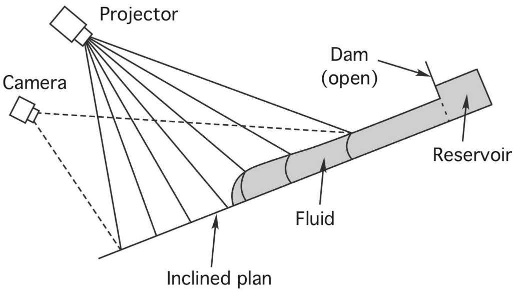

Figure 1. Sketch showing the experimental setup and the measurement system.

sluice gate. Using a high-speed digital camera, we then record how a fringe pattern projected on the flow surface is deformed, which makes it possible to measure the flow depth at any place on the surface.

More specifically, our system operates in the following way. A micro-mirror projector projects periodic fringe patterns of incoherent light onto the surface (see Sect. 3.3). We place the digital camera above the flow, but with an offset and a given inclination so that the camerawork angle differs from the projection angle. This camera records how the projected fringes are deformed by the free surface. From the optical point of view, fringe deformation induces a phase offset, which is directly proportional to the flow thickness. Thus, measuring flow depth boils down to measuring phase offset. A phase map is calculated using a 3–4 image algorithm (as described in Sect. 3.4 and 3.4.1). Fast flows require adapting this algorithm and in that case, we use a 1 image algorithm (see Sect. 3.5). Once the phase map obtained, the flow depth can be deduced by unwrapping the phase signal (see Sect. 3.6). This last step requires a calibration procedure, which is described in Sect. 3.7.

2.2 *Experimental facility*

The facility is made up of a metallic frame supporting an inclined plane, horizontal plane (run-out zone), and reservoir (see Fig. 2). This structure is 6 meters long, 1.8 meters wide, and 3.5 meter high. The 4.5 m long aluminium inclined plane can be inclined from 0° to 45° by the means of an electrical engine. Its position is accurately determined using a laser-meter to within 1 mm, which means that the accuracy on slope inclination is of the order of 10^{-2} °. The 6 mm thick aluminium plate is supported by a frame made up of 40 × 80 mm profiled aluminium beams that ensure rigidity.

A PVC reservoir of varying volume and shape is positioned at the top of the inclined plane behind the dam wall. The maximum capacity of the reservoir is 120 kg. The dam wall is composed of a $1.6 \times 0.8\,\mathrm{m}^2$ ultralight carbon plate. The 35 cm high sluice gate is opened within 0.8 seconds by two pneumatic jacks on each side. Using ultralight dam wall was needed to reduce dam-wall inertia, induced vibration, and jerk. The two jacks are fast rose by injecting 7 mPa pressured air. Two electromagnetic sensors have been located at the tip of each jack to control its position and reset the clock.

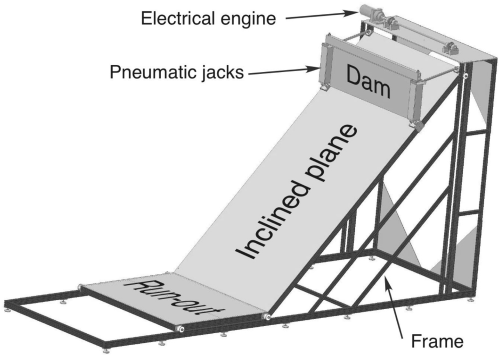

Figure 2. Schematic perspective of the facility.

The run-out plane has two functions: first, it collects the fluid flowing from the inclined plane, which makes the cleaning operations easier. Second—and this is the most important point—, the flowing material is forced to experience a transition from a flow regime to a deposition (run-out) regime. The 1.5 m long, 1.8 m wide run-out plane is maintained in a horizontal position and is connected to the inclined plane by a sealing plastic band. The projector and the camera are fixed on another frame, which is independent of the main frame.

2.3 *Experimental procedure*

A typical experimental run can be split into 4 phases. First, the fluid is prepared in advance (i.e., one or two days) and stocked in a 60 l drum to ensure sufficient resting time. Our viscoplastic fluid is a stable polymeric gel (Carbopol Ultrez). Polymer chains are vigorously mixed into a sodium-hydroxide/water solution at a given pH. This blend is left at rest for a long time so that all polymer chains have time to unroll and form a dispersion (repulsive interactions between chains). To ensure good light contrast, whitening Titanium Dioxide (TiO_2) is added when mixing Carbopol.

Second, the fluid is gently poured into the reservoir, while the inclined plane is kept in horizontal position. The material is then slowly mixed and its free surface is smoothed out by hand. A viscoplastic fluid does not flow if shear stresses are too low, which means that its free surface stays in the reservoir as it stands after pouring; there is no stress relaxation (viscoelasticity),

Figure 3. View on the sluice gate and the reservoir at the channel inlet.

nor creeping (viscosity), which would cause flattening of the free surface. The upper plane is then inclined at a given value and its position is checked using a laser-meter.

Third, the measurement device is calibrated. Calibration will be explained in detail in section 3.7. Just before starting the test, we collect a fluid sample and test it with a Bohlin CVOR rheometer to characterize its rheological properties.

Four, we lift up the sluice gate and the material starts accelerating and flowing. The surge motion is followed up by the digital camera. When there is no significant motion, we stop to record images. The material is then removed from the flume.

3 MEASUREMENT SYSTEM

3.1 *How to measure the free-surface variation with time?*

The crux of the difficulty in the dam-break experiments lies in the proper measurement of the free surface. We thought of different systems. Three criteria guided our choice. First, we needed a non-invasive system to avoid disturbing the free boundary. Second, our preference was on global methods that are able to capture the flow surface with a single pass in contrast with scanning methods, which are not well suited to providing snapshots. Third, we wished to develop a method consistent with high-speed acquisition rates.

Three global systems were considered:

1. A method, which involves projecting patterns onto the fluid surface. Pattern deformation is recorded by a camera. This method is described in section 3.2.
2. A stereoscopic system, with two cameras scrutinizing the same surface. This method performs well with surfaces of varying color and contrast since colored pixels can be used as reference points and tracked (Kraus and Waldhäusl 97). The height is computed by the taking the difference between two successive images recorded by the two cameras. Since our fluids are monochromatic, this method has been discarded.
3. A system based on the time of fly of emitted photons. Photons are emitted by a source, a number of which are back-scattered by the surface. The time between their emission and their reception provides an estimate of the travelled distance (Niclass et al. 2005). This method performs well only for static objects, but should be a promising technique for our purpose in the forthcoming years.

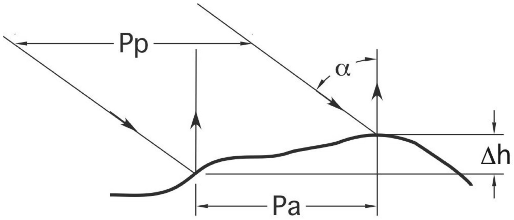

Figure 4. Projection of parallel lines on a surface and the retrieved height.

3.2 *Projecting patterns*

Measuring the shape of an object using the pattern projection can be broken down into three steps:

1. a given pattern is projected onto an object;
2. the object surface is imaged into a camera under an angle of incidence that differs from the imaging direction;
3. the surface height is retrieved from the image.

For the sake of simplicity, two parallel lines are projected onto a surface, as shown in figure 4. The height difference Δh can be then expressed as

$$\Delta h = \frac{\Delta p}{\tan \alpha}, \qquad (1)$$

where $\Delta p = p_p - p_a$ is the difference between p_p the projected lines onto the object and p_a the apparent line on the surface viewed by the camera; α is the angle between the projected lines and the camera.

This simple relationship emphasizes two points. First, the closer the projected lines p_p are, the greater the accuracy in Δh is. Second, the closer to 90° the angle α is, the better the accuracy in Δh is.

A problem with projecting lines is that any valuable information between two lines is lost. There is another technical problem related to the camera resolution: for two lines to be distinguished by the camera, there must be a minimum distance of three pixels, which imposes a lower bound on the accuracy of Δh according to equation (1).

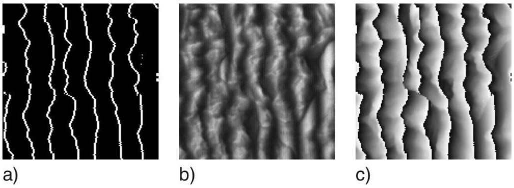

Figure 5. Comparison between: a) projection of lines, b) projection of fringes and c) the resulting phase map.

3.3 *Projecting fringes*

Cosine fringe patterns are projected instead of isolated lines. Information theory would say that we replace a 2 bit system into an 8 bit system, which should improve accuracy and robustness. Moreover, instead of relating height with light intensity, height is linked to fringe phase. The observed intensity at a given point (x,y) can be written as

$$I_k(x,y) = A_k(x,y) + B_k(x,y)\cos\phi_k(x,y), \tag{2}$$

where A_k and B_k represent the background and the modulation intensities and ϕ_k the phase. The phase varies within the interval $[0,2\pi[$.

Working with phase instead of intensity has the substantial advantage that alteration in surface reflectivity does not influence the outcome.

The imaging system consists of a digital camera coupled with a synchronized micro-mirror projector working at a maximum rate of 48 Hz. The 1000 × 1000 px CCD camera and the projector are synchronized by the frame grabber. The actual projection surface is $1.8 \times 1.1\ \mathrm{m}^2$. The main advantage of a micro-mirror projector (MMD) lies in its capacity to instantaneously project a given pattern. As mentioned in section 3, achieving high resolution in time and space requires global acquisition and projection. Compared to a laser interferometer, projecting fringe patterns with a MMD has also the advantage of versatility and safety. Any kind of pattern can be projected at any time and any rate. As an example, we can project images in 8 bit mode at a frequency of 150 Hz. There is, however, a price to pay when using a MMD instead of a laser interferometer: we have to use non-coherent light, which implies lower intensity. Perfect grabbed images would be characterized by intensity consistently with the intensity scale of a 8 bit camera; in other words, image intensity would range from 0 (deep black) to 255 (white). The technique is, however, quite robust since a phase map (see Sect. 3.4) can be can established using a limited range of 30 gray values.

The projector involves micro-mirrors. The light of a led is projected onto a micro-mirror device (MMD) composed of 1024 × 768 micro-mirrors oscillating between two positions; for one position, light is reflected through the projector lens, while for the other position, light is not reflected. It is a binary system: for a given pixel, light is on or off. A 8 bit grey level is achieved by changing the projection time of each micro-mirror.

At its maximum rate, the camera records an image within 20.7 ms, while the fringes are projected for 20.3 ms. A time lag of 0.1 ms separates two images. Special attention is paid to insuring that the whole projection occurs during the acquisition time and that there is no synchronization delay. This would have no consequence with projection continuously operating with time (as laser interferometry) but, as the MMD is a 2 bit projection system, relative intensity is controlled by the projection duration, which means that projection involves discretized time steps.

Capturing 48 images per second with a 1000 × 1000 px camera (i.e. 48 Mbytes/s) during time intervals as long as 10 minutes requires a CameraLink connection between the camera and the frame grabber. To store a huge amount of data within short intervals of time, we have implemented 4 hard disks in parallel. All the acquisition program has been developed using LabView.

3.4 *Phase map*

The phase map is only composed of the $\phi_k(x,y)$ term in equation (2). Optic convention is used here, high values (2π) are in white, whereas lower values (0) are in black.

Most algorithms for retrieving phase from an image or a series of images use either phase shifting , Fourier transform (Takeda et al. 1982), or wavelets (Liebling et al. 2004). The two first methods are explained in Sects 3.4.1 and 3.5. The phase map is often called the wrapped phase. During the first seconds of the test, a one-image algorithm is used and, after the flow has slowed down, a 3 or 4 image algorithm is used.

3.4.1 *Phase shifting*

Its principle consists in projecting $N \geq 3$ images of a fringe pattern shifted by $(i-1)2\pi/N$, with $i = 1\ldots N$ (Desmangles 2003). The phase can be analytically computed from the series of images. An example with a series of $N = 4$ images is given in figure 6, with the following intensities:

$$\left\{\begin{array}{lcl} I_1(x,y) & = & A + B\cos(\phi(x,y)), \\ I_2(x,y) & = & A + B\cos(\phi(x,y) + \frac{\pi}{2}), \\ I_3(x,y) & = & A + B\cos(\phi(x,y) + \pi), \\ I_4(x,y) & = & A + B\cos(\phi(x,y) + \frac{3\pi}{2}), \end{array}\right.$$

where

$$\phi = f(I_1,I_2,I_3,I_4) = \frac{I_4 - I_2}{I_1 - I_3}. \tag{3}$$

The phase map resulting from this method is accurate since it results from analytical calculation. A phase

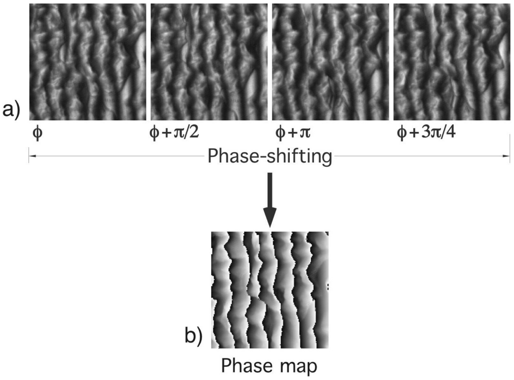

Figure 6. Phase shifting: a) with 4 images and b) the resulting phase map.

map can be extracted with each new image using the $N-1$ preceding ones.

The 3 fringe patterns can be projected at the same time using a red-green-blue (RGB) color coding. An independent phase map can be extracted with each new images. The idea is attractive, but requires a complicated and expensive setting (Jeong and Kim 2002).

The method based on 3 or 4 images is more appropriate when the fluid slows down and the relative motion between the first and the last images is less than a 1 or 2 pixels. This method is not suitable at earlier times, when the fluid is released because the displacement of the fluid between the first and the last images is too large. The resulting phase map is blurred and unusable. During the first instants of the test, the phase map must be computed with just one image; this computation can be done with a FFT algorithm, as explained in section 3.5 or with a wavelet algorithm.

3.5 *Fourier transformation profilometry (FTP)*

Fourier transformation profilometry (FTP) was first introduced by Takeda et al. (1982). The idea is to work in the frequency domain of the recorded images in order to filter and keep only the desired frequencies (Sansoni et al. 1999a).

In this subsection, we shall not explain how FTP works, but just provide some ideas on how we have implemented FTP in our setup. A cosine fringe pattern with 45° inclinations is projected onto the surface of the reference plane during the calibration, as shown in figure [see Fig. 7 (a), see also Sect. 3.7]. Two-dimensional Fourier transform analysis is then carried out on the recorded images, which consists in 5 points: first, the central peak related to frequencies close to zero is removed. Second, the frequency F_ϕ of the cosine fringe projected is located [see Fig. 7 (a)]. Third, the frequency map is filtered to keep only the desired values [see Fig. 7 c)]. Fourth, the frequency map is shifted to position F_{cos} at the center $F=0$ [see Fig. 7 (c)]. Fifth, the angle of the inverse FFT is computed, which provides us with the phase map of the reference plane [see Fig. 7 (e)].

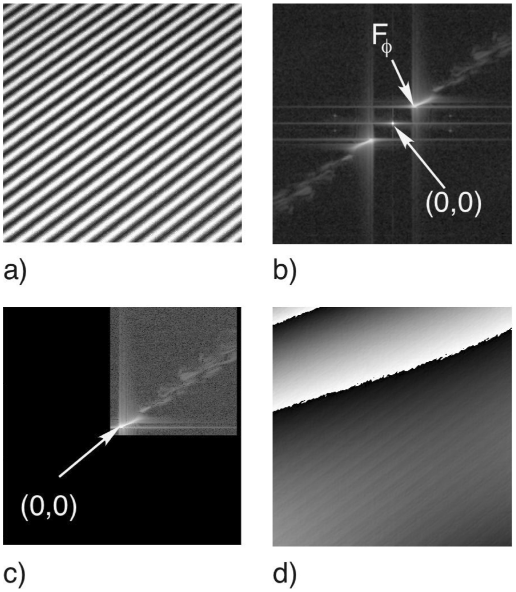

Figure 7. Reference plane: a) projected fringes, b) image in FFT domain with the frequency F_ϕ of the projected fringe, c) image filtered and shifted and d) reference plane phase map.

The same procedure is then repeated, during the test, with the recorded images except that the frequency map is shifted by F_ϕ (computed during the calibration). The wrapped phase is then obtained by subtracting the new phase and the phase of the reference plane [see Fig. 8 (f)].

FTP can be improved by removing image modulation so that the central peak of frequencies close to zero in the frequency map (related to the plane) is eliminated. This is achieved during the calibration procedure by shifting $N \geq 3$ fringe patterns by $(i-1)2\pi/N$ with $i=1\ldots N$, as explained in section 3.4.1. The modified image is then

$$I = I_1 - \frac{1}{N}\sum_{n=1}^{N} I_n.$$

FTP performs much better when the frequency of the projected cosine fringe is high and fringes are inclined at 45° in the recorded image because the cosine frequency F_ϕ in the FFT map is further away from the origin 0, filtering and shifting are more accurate.

Su and Chen (2001) discussed the influence of sampling in FTP. They emphasized that the recorded images as well as the discrete Fourier Transform (DFT)

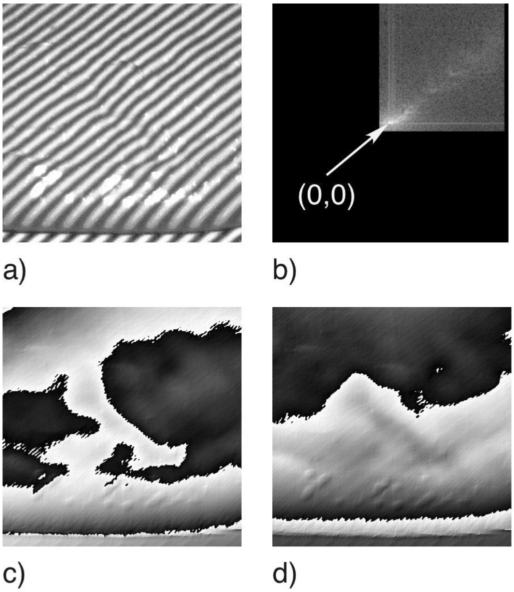

Figure 8. Object: a) projected fringes, b) object image filtered and shifted in Fourier domain c) resulting phase map and d) difference between the object phase map and the reference plane phase map.

are digital, whereas FTP theory is based on continuous Fourier transform. This inconsistency between theory and experience induces errors at high frequencies values. We are working to implement methods for reducing errors arising at high frequencies, even though we are convinced that this is a minor issue in our context (since our flows involve low frequencies most of the time).

FTP efficiency depends a great deal on filtering, i.e. which frequencies are kept or not. A good user can easily pinpoint frequencies that must be removed in order to obtain a more accurate phase map. Making this process automatic is, however, quite difficult.

It is almost impossible to know, in advance, when a phase-shifting algorithm can be used and can replace FTP. To avoid this issue, we project the 45° – inclined fringe with a phase shift of $2(i-1)\pi/N$ with $i=1\ldots N$. Both phase-shifting and FTP algorithms can then be used depending on the quality of their respective phase map.

3.6 *Phase unwrapping*

Once we have obtained the phase map, we can compute the height by unwrapping the phase map. The principle of phase unwrapping is fairly easy to understand in one-dimensional problems. Let us consider that we have a phase signal ϕ contained in the interval $[0, 2\pi[$ and we want to unwrap it. Every time the signal jumps from 0 to 2π, we add or subtract 2π depending on the derivative $\partial_x\phi$, as is illustrated in figure 9.

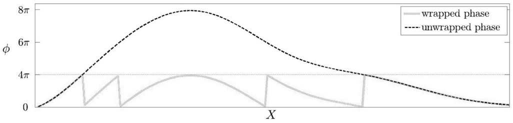

Figure 9. Example of phase unwrapping in 1D.

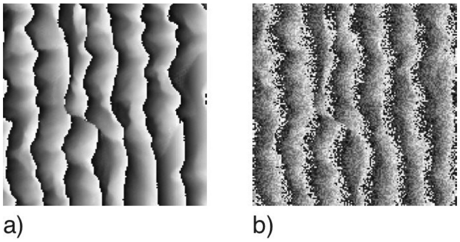

Figure 10. Phase map: a) original b) with noise.

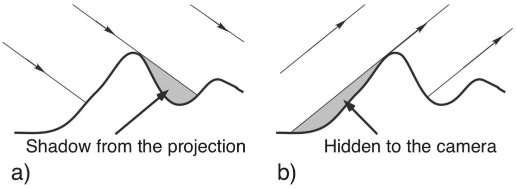

Figure 11. a) Shadow from the projector, b) hidden parts to the camera.

Without noise and shadow, phase unwrapping would have a unique solution. Any unwrapping algorithm tends to provide a proper approximate solution.

Noise blurs the sharp frontiers of the phase jump between 0 and π, as shown in figure 10.

Shadow regions appear when the projection does not enlighten all the surface or when a part of the surface is hidden to the camera, as sketched in figures 11 and 12. All the information in the shadow or hidden parts is lost. In order to obtain results as good as possible, one should be careful and avoid having shadow or hidden parts, while keeping the angle between the projecting and acquiring beams as close as possible to 90°.

There is not a single solution, but several approximate solutions. Two-dimensional phase unwrapping algorithms aim to find the best approximation.

In their book, Ghiglia and Pritt (1998) reviewed the main different strategies to phase unwrapping. They also provided eight valuable C++ routines illustrating those strategies. There are two different approaches to phase unwrapping: one is based on path-following methods or local methods and the other one is based on minimum-norm methods or global methods. The path-following methods starts at a given point in the phase

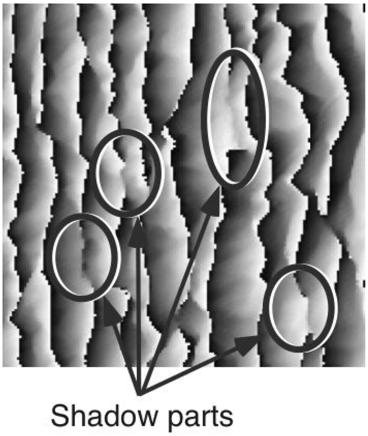

Figure 12. Shadow on an image.

map and computes the neighboring points by following a predefined path. The main difficulty is to choose 'the best path' to avoid shadowed or noisy parts in order to find the best approximation. Minimum-norm methods minimize the integral of the square difference between the gradients of the solution and the path obtained using different strategies. It is recommended to try the algorithm in the following order from the simplest and fastest ones to the more complex but slower ones.

1. Goldstein's branch cut algorithm, *path-following*,
2. Quality-guided algorithm, *path-following*,
3. Unweighted least-squares algorithm, *minimum-norm*,
4. Preconditioned conjugated gradient (PCG) algorithm, *minimum-norm*,
5. Mask-cut algorithm, *path-following*,
6. Multigrid algorithm, *minimum-norm*,
7. Flynn's minimum discontinuity algorithm, *path-following*, ,
8. Minimum L^p-norm algorithm, *minimum-norm*.

Better results are obtained with more complex algorithms. The last two algorithms are the most robust ones. We mainly use Flynn's method because its calculation time is much shorter than the Minimum L^p-norm. For our regular case, Flynn's method takes about 1'30" (Flynn 1997), while the Minimum L^p-norm requires 1 hr. However, using Flynn's algorithm on a 5 min sequence (14400 images) is quite impossible with a personal computer since it would take 15 days. One way for speeding up calculations is to run them on a computer cluster. To do so, we use the *distributed computing toolbox* from Matlab, with a cluster including up to 12 computers. Another way of reducing computation time is to unwrap the difference of the two phase maps (related to the flow and the reference plane) instead of computing the difference of the respective unwrapped phase, as shown in figure 13. The resulting map shows less jumps of 2π, which makes the reconstruction of the unwrapped phase easier, faster, and more accurate.

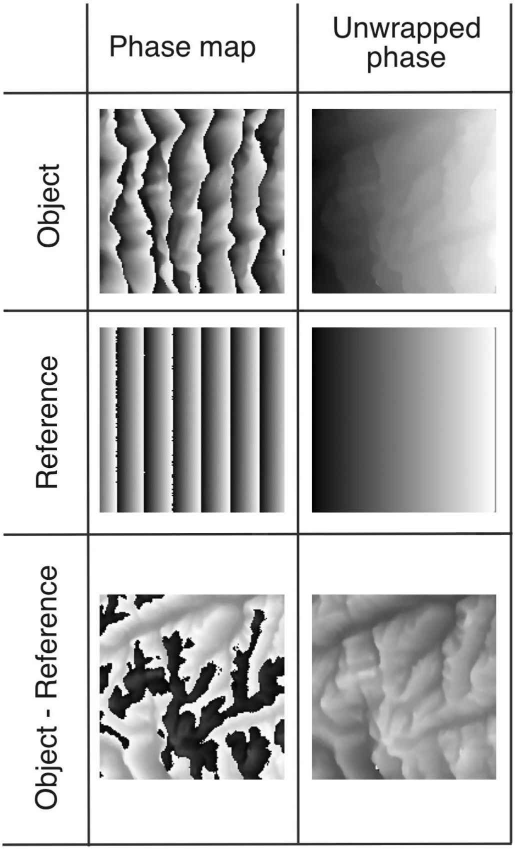

Figure 13. Unwrapping the difference of the object phase map and the reference phase map is equal to the difference of the unwrapped phases.

These algorithm have many input parameters, which have not only a large influence on the execution time, but also on the quality of the results. Various techniques have to be tested to evaluate the quality of the results and make them less dependent on the user. Even though we prefer Flynn's algorithm because of its accuracy, the other algorithms ought be tested because occasionally, they might give better results and require lower CPU time.

3.7 *Calibration*

Equation (1) give the height as a function of the angle α and the distance between two line P_p. Behind this equation, there is the following assumption: projection

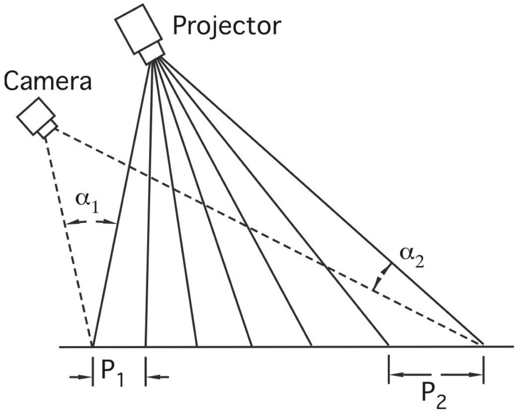

Figure 14. Variation of the angle α in a non-telecentric setup.

and acquisition are telecentric, which is not the case in our setup (Chen and Quan 2005). Figure 14 show how, in a non-telecentric setup, the angle α between the angle of projection and the angle of acquisition varies along the axe X; $\alpha_1 \neq \alpha_2$. The same also holds for the projected lines P_p and the apparent line P_a view by the camera; $P_1 \neq P_2$. A similar figure could be done along the Y-axis. Knowing the relative position of the camera, the projector and the inclined plane as well as the projection angle and the camera angle makes it possible to mathematically modify equation (1) and then have a height factor for each position (Desmangles 2003). This method requires accurately measuring the position of each elements of the setup, it is time-consuming, and does not take into account optical deformation. Instead of this method, we have chosen to use the more practical calibration based on a modified version of the virtual calibration plane method (Xiaoling et al. 2005).

The first step of the calibration is to project sharp patterns, such as squares, on the inclined plane to focus the projector and the camera. To check that the recorded images from the camera properly include the zone studied, the projection should envelop the acquisition zone, but should not be larger so that light power and projection resolution are optimized.

In order to relate the Cartesian coordinates XYZ of the plane with the unwrapped phase in the pixel coordinate ij, we need to calibrate our setup. A calibration plate, with gray circles of 2 cm in diameter and distant of 10 cm, is placed on the inclined plane at $z_0 = 0$. All fringe patterns, which will be used during the test run, are then projected on the calibration plane [see figure 15 (a)]. The module of the reference plane is computed [see figure 15 b)] and the position of the circle centers are found using a least-square approach [see figure 15 (c)]. The wrapped phase is referred as ϕ_{z_0} [see figure 15 (d)]. A relation between the plane XY_{z_0} and the camera coordinates ij is obtained using a piecewise linear interpolation.

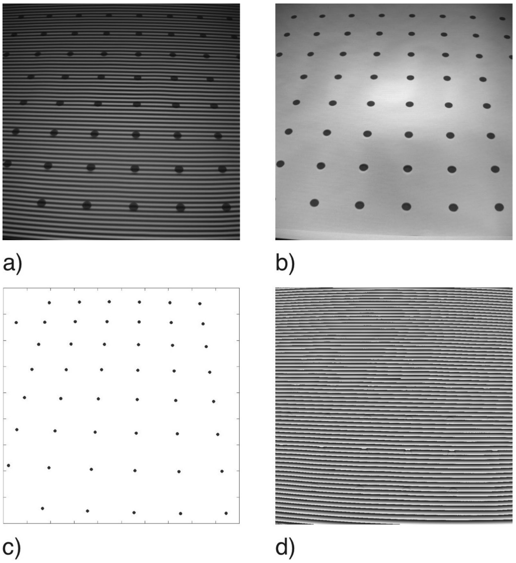

Figure 15. a) Projection of the fringe on the calibration plate, b) module with the calibration circles, c) position of the circle in the camera pixel coordinates and d) phase map of the calibration plane.

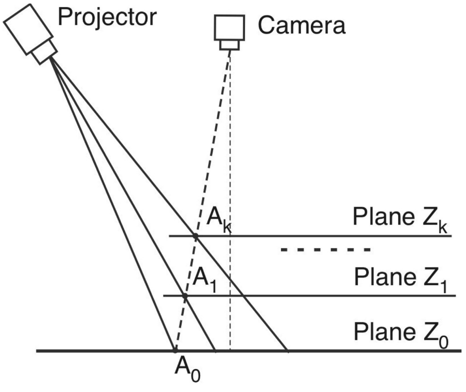

Figure 16. Calibration with virtual planes z_k.

All the circles cut by the frame of the image are removed since their center can not be properly calculated (information is partly lost). If they were kept, they would introduce distortion.

The same procedure is repeated k times with the calibration plate placed over the inclined plane at an elevation z_k, with $k = 1, 2, \ldots, K$ (see Fig. 16). A relation between the plane $XY_{z_k}(k = 1, 2, \ldots, K)$ and the camera coordinates ij is obtained using

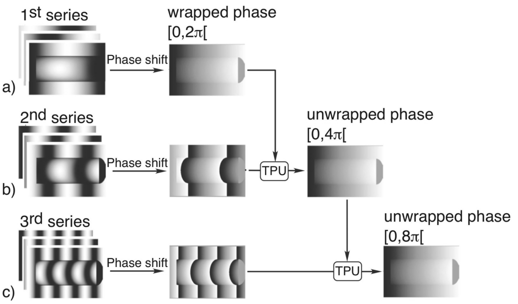

Figure 17. Temporal phase unwrapping: a) a first series of images with a large length wave, so the wrapped phase is set equal to the unwrapped one, is projected, b) the length wave is divided by 2 and a new series is projected, the unwrapped phase is obtained by looking up at the fist unwrapped phase, c) a new series is then projected with a length wave divided again by 2.

a piecewise linear interpolation. The corresponding wrapped phase ϕ_{z_k} is computed and the phase difference $\phi_{z_k} - \phi_{z_0}$ is unwrapped and denoted by ψ_{z_k}. ψ_{z_k} is not unique since $\phi_{z_k} - \phi_{z_0} \in [0, 2\pi[$. z_k is a function of $\varphi_{z_k} = \psi_{z_k} + j\pi$, with $j = 1, 2, \ldots$. A way to find j is explained in section 3.7.1. Once $\varphi_{z_k} = \psi_{z_k} + j\pi$ has been defined, a piecewise-linear-interpolation method is used to achiever Z-axis calibration. The unwrapped phases $\varphi_k (k = 1, 2, \ldots, K)$ at elevation $z_k (k = 1, 2, \ldots, K)$ are considered as reference phases. Based on the reference phases and their elevations z_k, every pixel height (Z-axis coordinate) can be obtained by linearly interpolating φ_k and z_k.

We end up with a calibration matrix M_{ijk}, which relates the value of the unwrapped phase φ_k in the pixel coordinates ij with the elevation z_k in the plane coordinates XY.

Compared with traditional way of calibration, this method reduces the hardware requirement of the system. It also simplifies the process of grabbing and processing data. Better accuracy is achieved by increasing the number of virtual calibrating planes z_k. The standard deviation error, using 5 virtual planes, is of the order of 1%.

3.7.1 *Temporal phase unwrapping*

Temporal phase unwrapping (TPU), presented in detail by Huntley and Saldner (1997), consists of unwrapping a phase with high sensitivity by means of others phases with lower sensitivity. First, a series of phase shifted images (see 3.4.1) is projected with a projected lengthwave L_{p_1} longer or equal to the surface to be measured. The wrapped phase ϕ_1 is then set equal to the unwrapped phase φ_1 [see figure 17 (a)]. Height resolution is low. A second series of phase shifted images is projected onto the surface, but with a lengthwave $L_{p_{\frac{1}{2}}}$ set to half the size of L_{p_1}. The wrapped phase $\phi_{\frac{1}{2}}$ is unwrapped by looking up at the wrapped phase φ_1 (see Fig. 17b)). This process is repeated n times until the desired $\phi_{\frac{1}{n^2}}$ is reached.

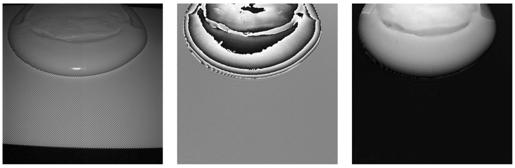
a) b) c)

Figure 18. Free surface at $t_2 = 2.4\,s$: a) 1 image used for the FTP algorithm, b) the wrapped phase and c) the height of the free surface.

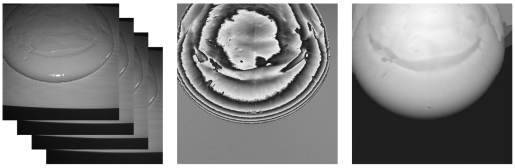
a) b) c)

Figure 19. Free surface at $t_2 = 38.5$ s: a) 4 images used for the phase-shift algorithm, b) the wrapped phase and c) the height of the free surface.

4 EXAMPLE

In this example, a 60 l volume of Carbopol Ultrez 10 at a solid concentration of 0.4% is released. The plane is inclined at 15°.

Figure 18(a) represents the grabbed image of the flow at time $t_1 = 2.4$ seconds. The wrapped phase [see Fig. 18 (b)] is obtained by a FTP. The unwrapped phase was computed using Flynn's algorithm. The final height is obtained using the calibration matrix [see Fig. 18 (c)].

The same test run but at $t_2 = 38.5$ seconds. The flow has slowed down and a 4 image phase-shift algorithm can be used. Figure 19 (a) shows the 4 images used to calculate the wrapped phase [see Fig. 19 (b)]. The wrapped phase is computed using Flynn's method. The height is shown in figure 19 (c).

5 CONCLUSION

New experimental facilities and procedures have been built to accurately measure the three-dimensional flow depth profiles in the dam-break problem. A mass of viscoplastic fluid is suddenly released by opening the dam sluice gate down a 4.5 m long inclined plane.

The three-dimensional flow-depth profiles are measured using a high-speed digital camera, which records how a fringe pattern projected onto the flow surface is deformed. To ensure uniform projection, a micro-mirror projector is used. The projector and the camera are synchronized at 48 Hz.

A cosine fringe pattern is projected onto the surface by the micro-mirror projector. A wrapped phase, from the recorded deformed images, is obtained using a 3–4 images phase shift algorithm or using a single image with Fourier transformation profilometry (FTP). The wrapped phase is then unwrapped using algorithms proposed by Ghiglia and Pritt (1998). The quality of the unwrapping algorithm depends on many parameters, which are user-dependent. Flynn's algorithm (Flynn 1997) tends to give the best time/accuracy ratio.

Height can be related to the unwrapped phase by a calibration matrix. The calibration matrix is obtained by placing a calibration plate at different elevation z_k and relating the pixel coordinates ij with circles on the plane to get the XY coordinates. At the same time, the phase of each z_k plane is recorded.

The 3 images phase-shifting method is used when the distance travelled by the surge is lower than one or two pixels between the first and the last image. Fourier transformation profilometry (FTP) is preferred when the flow is fast because only one image is needed. The drawback of this method is that a 'good' user dependent filtering is needed to remove parasitical frequencies.

Even though we are still improving the procedure to reduce the dependency of the results on the user, we are quite confident of the method expounded in this paper. The characteristics of the flow down the inclined plane (e.g., flow depth profile, front velocity) can be related with its rheogical properties. The precision on the surface height is of the order of 0.1 mm for a surface of $1.8 \times 1.2\,\text{m}^2$.

REFERENCES

Bartelt, P., B. Salm, and U. Gruber (1999). Calculating dense-snow avalanche runout using a Voellmy-fluid model with active/passive longitudinal straining. *J. Glaciol. 45*, 242–254.

Chen, L. and C. Quan (2005). Fringe projection profilometry with nonparallel illumination: a least-squares approach. *Optics Letter 30*(16), 2101–2103.

Desmangles, A.-I. (2003). *Extension of the fringe projection method to large objects for shape and deformation measurement*. Ph. D. thesis, EPFL.

Flynn, T. (1997). Two-dimensional phase unwrapping with minimum weighted discontinuity. *Journal of the Optical Society of America 14*(10), 2692–2701.

Ghiglia, D.C. and M.P. Pritt (1998). *Two-dimensional phase unwrapping: theory, algorithms, and software.* Wiley-Interscience. Wiley, cop.

Griffiths, R. (2000). The dynamics of lava flows. *Annu. Rev. Fluid Mech. 32*, 477–518.

Hogg, A. and D. Pritchard (2004). The effects of hydraulic resistance on dam-break and other shallow inertial flows. *J. Fluid Mech. 501*, 179–212.

Huang, X. and M. garìa (1997). A perturbation solution for Bingham-plastic mudflows. *Journal of Hydraulic Engineering 123*, 986–994.

Huntley, J.M. and H.O. Saldner (1997). Shape measurement by temporal phase unwrapping: comparison of unwrappingalgorithms. *Meas. Sci. Technol. 8*, 989–992.

Iverson, R. (1997). The physics of debris flows. *Rev. Geophys. 35*, 245–296.

Jeong, M.-S. and S.-W. Kim (2002). Color grating projection moire with time-integral fringe capturing for high-speed 3-D imaging, *Opt. Eng 41*(8), 1912–1917.

Kraus, K. and P. Waldhäusl (1997). *Manuel de photogrammérie, principes et procédés fondamentaux*. Hermes.

Liebling, M., T. Blu, and M. Unser (2004). Complexwave retrieval from a single off-axis hologram. *J. Opt. Soc. Am. A 21*(3), 367–377.

Niclass, C., A. rochas, P. Besse, and E. Charbon (2005). Design and characterization of a CMOS 3D image sensor based on single photon avalanche diodes. *Journal of Solid-State Circuits*, 1847–1854.

Parker, G., Y. Fukushima, and H. Pantin (1986). Selfaccelerating turbidity currents. *J. Fluid Mech. 171*, 145–181.

Pritchard, D. (2005). On fine sediment transport by a flood surge. *J. Fluid Mech. 5343*, 239–248.

Ritter, A. (1892). Die Fortpflanzung der Wasserwellen. *Zeit, Vereines Deutsch. Ing. 36*(33), 947–954.

Saint Venant, B. (1871). Théorie du mouvement non permanent des eaux, avec application aux crued des rivières et àl' introduction des marées dansleur lit. *C. R. Acad. Sci. Paris Sér. I 173*, 147–154– 237–240.

Sansoni, G., M. Carocci, and R. Rodella (1999). Three-dimensional vision based on a combination of gray-code and phase-shift light projection: analysis and compensation of the systematic errors. *Appl. Optics 38*, 6565–6573.

Su, X, and W. chen (2001). Fourier transform profilometry: a review. *Optics and Lasers in Engineering 35*, 263–284.

Takeda, M., H. Ina, and S. Kobayashi (1982). Fourier-transform method of fringe-pattern analysis for comuter-based topography and interferometry. *Journal of the Optical Society of America 72*(1), 156–160.

Xiaoling, Z., L., Yuchi, Z. Meirong, N. Xiaobing, and H. Yinguo (2005). Calibration of a fringe projection profilometry system using virtual phase calibrating model planes. *J. Opt. A: Pure Appl. Opt 7*, 192–197.